CrystEngComm

PAPER

View Article Online
View Journal | View Issue

CrossMark click for updates

Cite this: *CrystEngComm*, 2017, **19**, 975

Zinc diphosphide nanowires: bismuth nanocrystal-seeded growth and their use as high-capacity lithium ion battery anodes†

Jee-Yee Chen, Li-Chu Chin, Guo-An Li and Hsing-Yu Tuan*

Received 20th October 2016,
Accepted 7th January 2017

DOI: 10.1039/c6ce02206e

rsc.li/crystengcomm

For the first time, binary lithium-reactive zinc diphosphide (ZnP_2) nanowires were synthesized *via* bismuth-seed growth at 400 °C *via* a solvothermal route. The synthesized ZnP_2 nanowires are single crystals with diameters ranging from 10 to 50 nm and have a precise orthorhombic structure without impurity phases. From SEM and HRTEM images, the lengths of the nanowires over several micrometers could be observed. The effect of reaction parameters, including temperature and seed to precursor ratio, on the quality of reaction products has been systematically investigated. We used ZnP_2 nanowires as an anode material for lithium batteries since ZnP_2 has a much higher theoretical capacity of 1581 mA h g^{-1} than that of commercial graphite (372 mA h g^{-1}). The capacity of the first discharge cycle was 1415 mA h g^{-1} at 0.3C (1C = 1581 mA h g^{-1}) with high Coulombic efficiency up to 89%. The discharge capacity was maintained at 1066 mA h g^{-1} after 500 cycles, showing good capacity retention and long lifespan. With these merits and excellent electrochemical performance, ZnP_2 nanowires clearly are a promising anode material for lithium ion batteries.

Introduction

The demand for energy storage devices is growing rapidly, particularly for high-energy-density-storage systems.[1–4] Lithium ion batteries (LIBs) are the most widely used portable storage devices due to several merits such as long cycle life, high energy density, and good rate capability.[5,6] There are three main types of materials as anode materials for lithium ion batteries. The first to be introduced was graphite (372 mA h g^{-1}) in 1991.[7] Later on, in order to pursue higher-capacity alternative materials, nanostructured carbon-based materials and metal oxides have attracted attention.[8–12] Unfortunately, these two types of materials have low electric conductivities and low capacities. Furthermore, Ge, Sn, Si and P (ref. 13–17) appear to react reversibly with large amounts of Li, but their retention capacities are poor due to large volume changes (*e.g.*, >300% for Si and Ge) during the charge/discharge process. Recently, numerous studies have been carried out to tolerate the mechanical stress of Ge,[18–25] Sn (ref. 18–21) and Si (ref. 26–30) systems, and obtain significantly improved battery performance. However, compared to Ge, Sn and Si systems, little effort has been devoted to the phosphorus-based system.

Zinc phosphide systems (Zn_yP_x) have attracted much attention because of their extraordinary inherent characteristics such as rich binary phases (Zn_3P_2, ZnP_2 and ZnP_4), a small energy band gap (1.6 eV), and their high capacity, low and flat potential profile.[31–45] In addition, because of direct P–P bonding, phosphorus atoms are able to exist as single anions or larger polyphosphate anions and form different binary phases with compositions from zinc-rich to phosphorus-rich. In the zinc phosphides system, both zinc and phosphorus react with lithium ions, and both contribute to the capacity (zinc is 815 mA h g^{-1}, and phosphide is 2596 mA h g^{-1}). Bhushan and Catalano successfully designed polycrystalline Zn_3P_2 Schottky barrier solar cells with energy conversion efficiencies as high as 5.96%.[46] Different types of nanostructures of Zn_3P_2 have been studied,[47] leading to much improved lithium ion batteries since Zn_3P_2 is more accessible to be demonstrated.[48]

Phosphorus-rich ZnP_2 has greater theoretical lithium capacity (1581 mA h g^{-1}) than that of zinc-rich Zn_3P_2 (1241 mA h g^{-1}). However, most of ZnP_2 was synthesized directly by a high energy ball-milling technique[49] or a chemical vapour phase transport method[43] carried out at high temperature and complex reaction conditions, and the resulting product morphology was difficult to control. Furthermore, the performance in the LIB was not good, and the lifetime of the LIB was also short. The serious agglomeration of the product by ball-milling reduced the surface area to react and diffuse the ion. In other words, this problem may diminish the

Department of Chemical Engineering, National Tsing Hua University, Hsinchu 30013, Taiwan. E-mail: hytuan@che.nthu.edu.tw

† Electronic supplementary information (ESI) available. See DOI: 10.1039/c6ce02206e

conductivity and damage the performance of the electronic experiment. Blending active materials with carbon for the ball milling was conducted to solve the problem. In 2008, Park and Sohn improved the conductivity through blending ZnP_2 powder with a massive amount of carbon. However, the half-cell lithium ion battery's lifetime was less than 50 cycles, and the capacity dropped to around 400 mA h g^{-1}.[49]

In the view of this, we demonstrated the synthesis of single crystalline ZnP_2 nanowires for the first time using a mixture of diethylzinc solution (1 M in hexane), tri-*n*-octylphosphine (TOP) as precursors, and bismuth (Bi) precursor as metal seed sources *via* metal-seed growth using a solvothermal route. Importantly, when tested as the integrated anode for a half-cell lithium battery, the material showed a high reversible capacity of nearly 1415 mA h g^{-1} at 0.3C rate (1C = 1581 mA h g^{-1}), which was 3.8 times higher than that in the theoretical capacity of graphite (372 mA h g^{-1}). A long lifetime of over 500 cycles has been maintained with a high rate capacity.

Results and discussion

ZnP_2 nanowire synthesis

Bi-seeded ZnP_2 nanowires were fabricated by heating from room temperature to 400 °C by reacting diethylzinc and tri-*n*-octylphosphine in the presence of a Bi precursor in a titanium reactor by a solvothermal route. This method is analogous to a metal-seeded solution–liquid–solid process.[50–57] After the unconverted precursor was removed with chemically stable ZnP_2 nanowires, the material was finally obtained. The X-ray diffraction (XRD) pattern of the nanowire powder is shown in Fig. 1. All of the fingerprint diffraction peaks were assigned to pure orthorhombic ZnP_2 (JCPDS card no. 44-1237 (ref. 58)). The main difference between Zn_3P_2 and ZnP_2 was that reflection peaks of Zn_3P_2 (JCPDS card no. 47-1441,[59] 27.109° and 45.105°) and ZnP_2 (29.086° and 48.307°) were at different angles and different related strengths. Thus, in the Fig. 1, no other patterns, such as Zn_3P_2 or ZnP_4, were found.

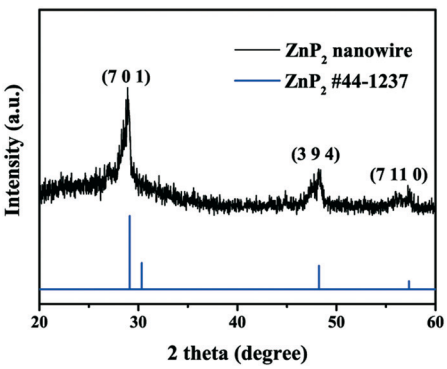

Fig. 1 Bi-seeded ZnP_2 nanowires produced with diethylzinc solution, TOP and Bi precursor at 400 °C for 15 minutes. The XRD pattern for ZnP_2 NW products.

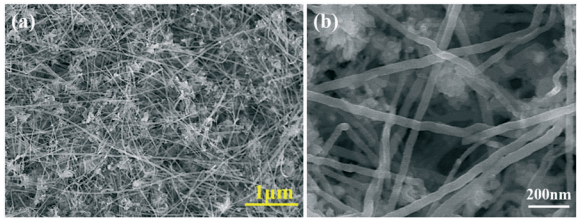

Fig. 2 Bi-seeded ZnP_2 nanowires produced with diethylzinc solution, TOP and Bi precursor at 400 °C for 15 minutes. (a and b) Different magnification SEM images to observe the surface morphology of ZnP_2 NW products.

In order to confirm the morphology of the product, the products were observed with a scanning electron microscope (SEM) (Fig. 2(a and b)). From the SEM images, it could be observed that the nanowires with lengths over several micrometers were entangled together. Synthesized by a metal-seeded solvothermal route, the diameters of most nanowires were controlled between 10 to 50 nm. The nanowires' growth was more rugged as observed from the high-magnification SEM images as shown in Fig. 2(b). As shown in transmission electron microscopy (TEM) images (Fig. 3), the crystalline structure and the morphology of ZnP_2 nanowires was developed and analyzed by the corresponding fast Fourier transform (FFT) diffraction pattern *via* HRTEM. The selected area electron diffraction (SAED) pattern and the fringe distance corresponded to ZnP_2. The d-spacing (JCPDS card no. 44-1237, 3.066 Å, 2.9438 Å and 1.8871 Å) once again confirmed that the nanowire was ZnP_2. The magnified image of the SAED pattern (Fig. S1†) (Fig. 3(a)) shows that both (1 0 5) and (7 0 1) appear on the sample. For further evidence, the energy dispersive spectrometer (EDS) was used as shown in Fig. 4(a–c). In Fig. 4(a), the TEM image and the mapping result clearly displays the Bi nanoparticles as the tips of the grown nanowires. Fig. 4(a) provides evidence that the growth of ZnP_2 nanowires undergoes a classic Bi-seeded nanowire growth. Furthermore, Fig. 4(b) is the result of the spectrum scanning for the nanowires.

The TOP-formed ligand on the nanowires' surface can be clearly seen in the image. Moreover, Fig. 4(b) shows that the ratio of Zn to P for the nanowire was 3 : 7. From the results and the image, it can be observed that elemental P was contained in more than expected amounts, which might be

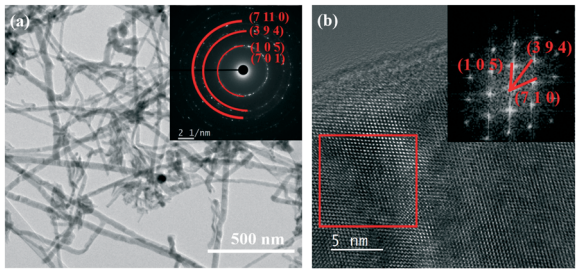

Fig. 3 (a) TEM and (b) HRTEM images of ZnP_2 NWs. Inset shows the FFT pattern.

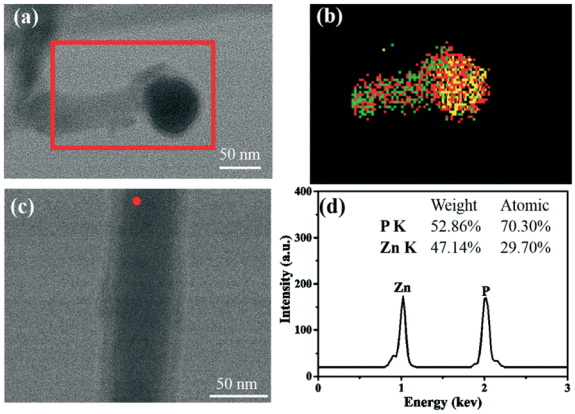

Fig. 4 (a and b) HRTEM of a ZnP_2 nanowire and tip with EDS mapping. Yellow is Bi, red is P, and green is Zn. (c and d) EDS spectrum scanning (the red dot) element by HRTEM image of ZnP_2 nanowire.

due to the ligand on the surface as shown in Fig. 4(a). That is, the ratio of Zn and P was about 1 : 2 in the nanowire.

Different concentrations of precursor and reaction temperatures were accomplished in order to analyze the optimized conditions for the growth of ZnP_2 nanowires. A series of experiments was explored to investigate the relationship between the precursor for zinc and seed, and zinc and phosphide. In Fig. 5(a)–(d), the different proportion of the zinc precursor and the seed had different types of morphologies for the nanowire, while keeping the same ratio of the precursor of zinc and phosphide. In Fig. 5(a), the morphology was mostly the Bi seeds aggregation due to the massive seed precursor concentration. The seed not only dissolved zinc and phosphide to grow the nanowire, but also dissolved itself for the excess concentration under the reaction temperature. When the concentration of the seed was low, much improvement in the production of the nanowires was observed. However, compared to Fig. 5(c) and (d), Fig. 5(d) showed fewer nanowires but more nanoparticles since the concentration of the seed was low, and the precursor of zinc and phosphide were excessive. When the ratio of the seed to the zinc precursor was 1 : 2000, a superior production of the nanowire was observed, as shown in Fig. 5(c).

Synthesis of ZnP_2 nanowires at temperatures of 320 °C to 430 °C are shown in Fig. 6(a)–(d). Among all the reaction temperatures, 400 °C (Fig. 6(c)) was found to be the optimum reaction temperature considering the purity of ZnP_2 nanowires obtained at the temperature. At lower temperatures of 320 °C and 350 °C (Fig. 6(a and b)), only a small amount of the precursor decomposed. The nanowires were less formed when the temperature was reduced. On the other hand, when the temperature was increased from 420 °C to 430 °C (Fig. 6(d)), the nanowires grew with an extreme amount of crystallinity, and some micrometer-sized particles had formed. Several studies have suggested that the temperature-dependent growth of the performances of nanowires may be related to the concept of homogeneous nucleation reactions. The poor density of nanowires may be due to the fact that the diffusion rate and mobility of ions were restricted. In other words, the synthesis is based on competition between the kinetics of particle nucleation to nanowire growth.[57,60] As a result, when the reaction temperature rose from 420 °C to 430 °C, the formation of the particles showed that the rate of the nucleation overcomes the rate of crystallization of the nanowires. On the contrary, precursor ions prefer to diffuse in the already-formed seeds, rather than in the bare substrate. Therefore, the reaction temperature appears to be the critical parameter to grow high-quality nanowires. In another series of experiments, the ratio between the precursor of zinc and phosphide was explored, and the results are shown in Fig. 7(a)–(c) for SEM images and Fig. 7(d) for the XRD. Compared to the differences of various ratios of seed to zinc, the effects between the differences of various ratios of zinc and phosphide were minor. However, among the conditions shown in Fig. 7(a)–(c), the conditions displayed in Fig. 7(c) resulted in the fewest nanoparticles. Moreover, in Fig. 7(d), the XRD image revealed that such conditions had the purest morphology of ZnP_2. Other conditions showed Zn_3P_2 (JCPDS card no. 47-1441,[59] 27.109° and 45.105°) patterns. Moreover,

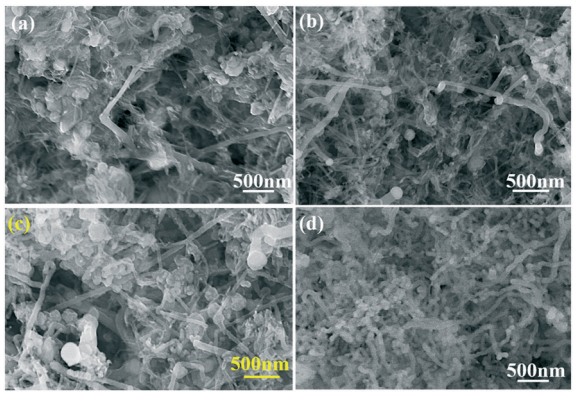

Fig. 5 SEM images of ZnP_2 nanowires synthetized under various ratios of seed (Bi) to zinc precursor (a) 1 : 625 (b) 1 : 1000 (c) 1 : 2000 (d) 1 : 4000 at 350 °C.

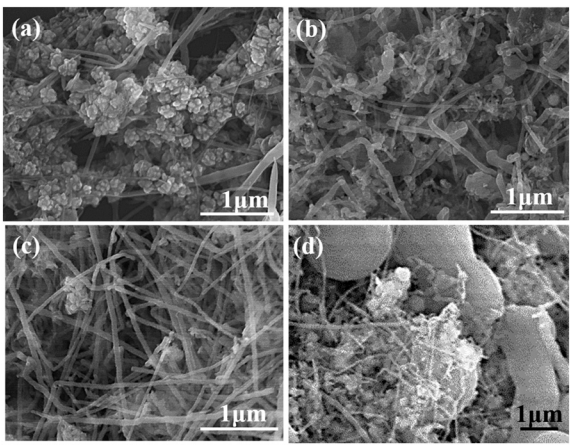

Fig. 6 SEM images of ZnP_2 nanowires synthesized under various reaction temperatures: (a) 320 (b) 350 (c) 400 (d) 430 °C.

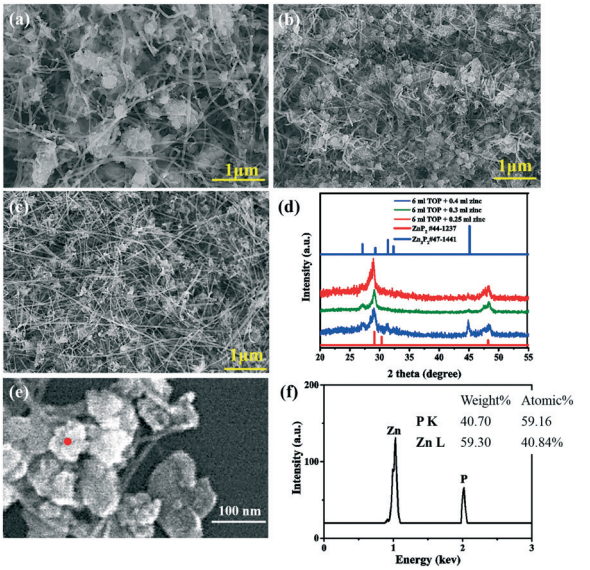

Fig. 7 SEM images of ZnP_2 nanowires synthesized under various ratio of phosphide and zinc precursor (a) 6 mL TOP + 0.4 mL zinc (b) 6 mL TOP + 0.3 mL zinc (c) 6 mL TOP + 0.25 mL zinc (d) the XRD patterns (e and f) EDS spectrum scanning (the red dot) element for a SEM image of nanoparticles.

lesser zinc precursor concentration resulted in fewer Zn_3P_2 particles and the signal strength of Zn_3P_2 pattern was reduced. For the mechanism of ZnP_2 nanowire growth, different reaction temperatures and concentrations of precursors were additionally examined as important factors. Fig. 7(f) shows the EDS spectrum for the particle. The weight ratio of the particle between Zn and P was 3 : 2, and the mole ratio was 2 : 3. The reason for the higher P atomic ratio than expected might be attributed to the ligand, which was composed of P. However, the mole ratio was close to Zn_3P_2, and was far from ZnP_2. In addition, considering the evidence from the SEM images, XRD pattern and EDS spectrum element scanning, the nanoparticle might be Zn_3P_2.

Lithium-ion battery assembly and electrochemical characterization

To confirm the electrochemical properties of the ZnP_2 nanowires were investigated by installing them into a coin-type half-cell. This method not only provided a typical arduous electrode preparation process, but also assured a large available lithium-reactivity surface and good electric conductivity contact. The cycling performance of ZnP_2 nanowires *versus* Li metal was analysed at a current density of 0.1C (1C = 1581 mA h g^{-1}) in the first cycle and 0.3C in the rest of the cycle in the voltage window of 0.02–2.5 V. For the first charge and discharge capacities, the capacities were 1575 and 1415 mA h g^{-1}, respectively, and the Coulombic efficiency was 89%. The irreversible capacity loss in the first cycle was possible because of the formation of a solid electrolyte interface (SEI) layer. The SEI layer resulted from electrolyte decomposition, which may impede lithium ion transport and increased internal resistance.[61] As a result, a slow C rate would be needed. During the subsequent cycles, the capacity retention of as-prepared ZnP_2 nanowires maintained a great level of Coulombic efficiency at ~99%, showing good capacity retention. In other words, the electrochemical experimental evidence demonstrated the ZnP_2 nanowires as an anode material for lithium ion batteries. Furthermore, the capacity of the 500th cycle still remained 1066 mA h g^{-1}, with an average capacity decay of 0.1352% per cycle showing excellent capacity retention. Moreover, Fig. 8(b) and (c) reveal the CV curves of the

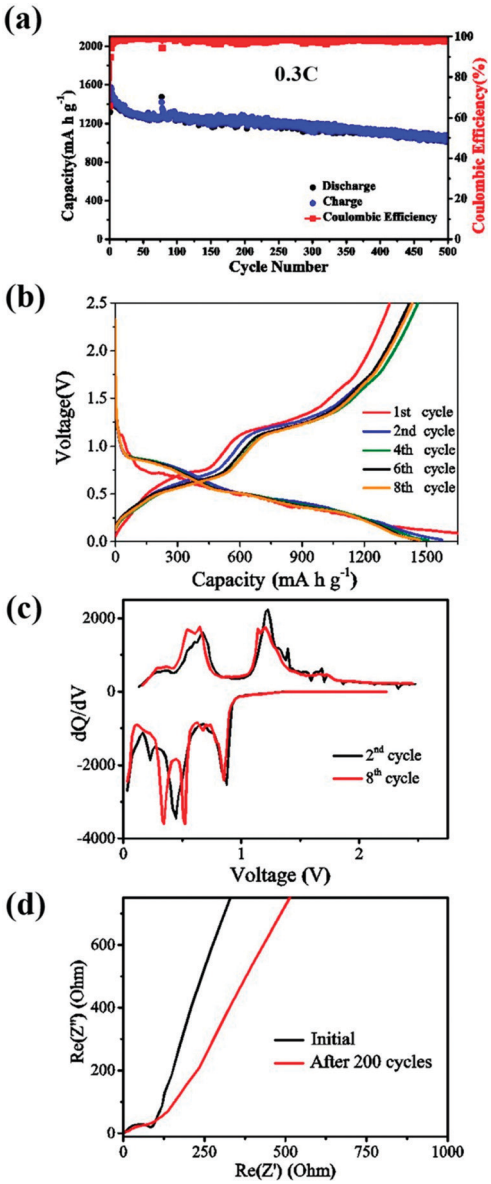

Fig. 8 (a) Charge/discharge cycle performance of calcinated ZnP_2 nanowires at a rate of 0.3C between 0.01 and 2.5 V. (b) Galvanostatic charge/discharge profiles of ZnP_2 nanowire at 0.1C for the first cycle, and 0.3C for the 1st, 2nd, 4th, 6th and 8th cycles. (c) Differential capacity of the 2nd and 8th cycles of ZnP_2 nanowires at a rate of 0.3C between 0.01 and 2.5 V (d) electrochemical impedance spectroscopy of calcinated ZnP_2 nanowire electrode with the first and after 200 cycles of charge/discharge cycling test.

1st, 2nd, 4th, 6th and 8th cycles and the differential capacity of the 2nd and 8th cycles, respectively. In addition to the first cycle, the charge reaction plateau occurred at 0.6 V, and the subsequent cycles' voltage profile had a plateau at 0.75 V. As shown in Fig. 8(c), the main difference between the 2nd and 8th cycle was that the differential capacity showed a plateau at 0.5 V in the 2nd cycle, whereas it was split to 0.65 V and 0.4 V in the 8th cycle. This is because the insertion reaction for Zn and Li has two steps: $ZnP_2 \rightarrow LiZnP + LiP \rightarrow Li_3P + LiZn$. The 1st and 2nd cycle are still on the activation barrier for the material and Li (0.5 V).[62] On the 3rd cycle, the activation peak begins to split into the two steps of the insertion reaction (0.6 V and 0.4 V). Until the 8th cycle, the peak of the two steps equally split. On the following cycles, the insertion reaction went through two steps, which have the same peaks as the 8th cycle. This plateau referred to the lithium insertion reaction, which formed LiZn alloys, while the plateau[48,49] at 0.8 V referred to Li_3P ($7Li^+ + 7e^- + ZnP_2 \rightarrow LiZn + 2Li_3P$). During the reaction, the intermediate phases can be formed even though they were not identified. On the other hand, two plateaus at 1.25 and 0.75 V in the cathodic scan were correlated to the reaction of delithiation of Li_3P and LiZn ($LiZn + 2Li_3P \rightarrow 7Li^+ + 7e^- + ZnP_2$). Moreover, to identify the capacity contribution between Zn and P, the plateau of the phosphide lithium insertion reaction (shown in Fig. 8(b)) at 1.25 V was maintained from 700 to 1300 mA h g^{-1}, and the zinc lithium insertion reaction plateau at 0.75 V was maintained from 500–200 mA h g^{-1}. The capacity contribution ratio between zinc and phosphide was about 1 : 2. As shown in the Nyquist plots (Fig. 8(d)), EIS analysis was employed to explore the ZnP_2-based electrodes interfacial electrochemical behavior during the cycling test with different charge/discharge cycles for 0.1C at frequencies from 10 kHz to 10 MHz. The semicircle in the ESI test at the high frequency region began from 0 Ω, both in the initial non CV cycle and after 200 cycles coin cells. In this case, the resistance for Li^+ ion that defused in the electrolyte solution was small enough to be neglected. In other words, the electrolyte solution was suitable for the half-cell battery.[63] The semicircle, also called charge transfer resistance, appeared while frequency decreases, indicated when electrode potential is barring its equilibrium value is polarized at open circuit. In the image, the electrode had the smaller diameter of the semicircle after 200 cycles, which indicated that the fresh electrode's charge transfer resistance is larger. During cycling, the electrode structure transformation is favourable for lithium ion diffusion and electron transfer.[64] The sloping region indicates diffusion resistance of the electrolyte ions into the electrode as the frequency decreases, which is called Warburg impedance. The slope decreased at the low frequency region after 200 cycles, which may be due to the generation of facile lithium diffusion channels that have decreased diffusion resistance. The reason might be associated with the formation of Li ion conductive matrix Li_3P and LiZn during charge/discharge.[65]

Fig. 9(a) shows the high rate capacities measured by charge/discharge rates from 0.1C to 4C. The capacity of

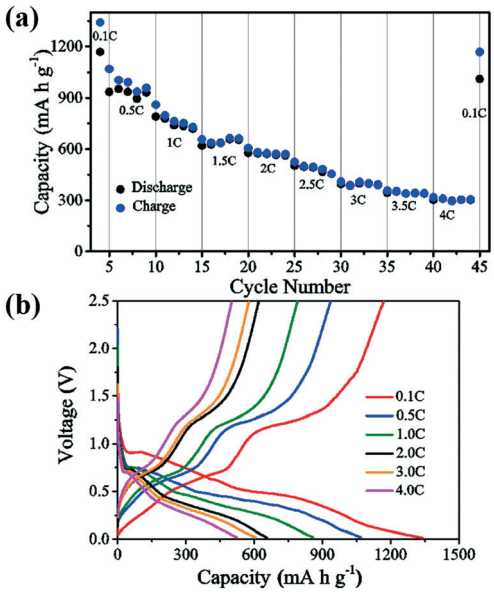

Fig. 9 In high rate tests, (a) rate capability test including 0.1, 0.5, 1, 1.5, 2, 2.5, 3, 3.5 and 4C with multiple cycle execution. (b) Galvanostatic charge/discharge profiles of ZnP_2 nanowires at 0.1, 0.5, 1, 2, 3 and 4C.

ZnP_2 nanowires was impressive since they had very good retention at different rates. Moreover, the capacity of 1045 mA h g^{-1} was observed again when the current rate was 0.1C once again. Moreover, the performance in long cycles (700 cycles) at a high rate (3C) is present in Fig. S2.† The CV curves of different C rates are shown in Fig. 9(b). The capacity contribution from both Zn and P at high rates was less than that at low rates. However, considering 1C for example, the ratio of contribution of zinc to phosphide was 1 : 1 (250 : 250). In other words, the capacity contributed from zinc in the high rate.

Experimental

Chemicals

All reagents were used as received. Bismuth(III) 2-ethylhexanoate was purchased from Alfa Aesar. Oleylamine (OLA, 70%), toluene (99.99%), ethanol (99.99%), tri-*n*-octylphosphine (TOP, 90%), diethylzinc solution (1 M in hexane), and poly (acrylic acid) (PAA, average MW ~100 000) were purchased from Sigma-Aldrich. Celgard membrane, Li metal foil (99.9%), Cu metal foil (0.01 mm), electrolyte (1 M $LiPF_6$ in fluoro-ethylene carbonate/diethyl carbonate (FEC/DEC) (1 : 1 vol%)), $LiFePO_4$ cathode material, Super P carbon black, coin cells (CR2032), were obtained from SYNergy ScienTech Corp. Al laminated film and a metallic strip terminal for pouch cell assembly were purchased from MTI Corp. All the materials were used without further purification.

ZnP_2 nanowire synthesis

ZnP_2 nanowires were synthesized in a 10 mL titanium reactor, and transferred into an argon-filled glove box to free the

reactor from air. The precursor solution was injected and the reactor was filled with only argon. Furthermore, 6 mL of TOP was injected as the phosphorus precursor with 2.5 mL of diethylzinc solution (1 M in hexane) as the zinc precursor. Bismuth 2-ethylhexanoate in OLA with a concentration 0.0025 M was prepared as seeds for nanowire growth. For the reactant, a 2000 : 1 of zinc/Bi precursor mole ratio was used in the reaction. After the precursor was injected into the reactor in the glove box, the reactor was taken out of the box. The reactor was then heated up from 400 °C to 410 °C. After the temperature was steady at 400 °C for 15 minutes, the reactor was quenched by a water batch. Finally, when the reactor was cooled to the room temperature, the ZnP_2 nanowires were taken out of the reactor for further analysis.

Lithium-ion battery assembly and electrochemical characterization

Before the preparation of the slurry for the half-cell battery, the product was heated to 380 °C for 2 hours in argon in order to remove the oil-liked ligand on the nanowires' surfaces. After the oil-liked ligand was removed, the homogeneous slurry for the anode electrode was then prepared by mixing active materials (ZnP_2 nanowire, 70 wt%) with 20 wt% of Super-P and 10 wt% of PAA binder dispersed in ethanol, which continued to spread on the copper foil. Prior to being assembled, the electrode was dried at 120 °C under argon gas to remove solvent and residual water. The electrode was cut into a 12 mm diameter circle shape for the coin cell after being densely pressed with a rolling press machine. A composite electrode, a separator soaked in an electrolyte, and a lithium metal foil were contained in the coin-typed half-cell (CR2032) and were all prepared in a glove box. The electrolyte solution was 1 M $LiPF_6$ dissolved in fluoroethylene carbonate/diethyl carbonate (FEC/DEC) at 1 : 1 vol%. Electrochemical performance of the ZnP_2 nanowires was tested using Maccor Series 4000 instruments.

Characterization

The morphologies of the ZnP_2 nanowire products were characterized *via* scanning electron microscopy (SEM), energy-dispersive X-ray spectroscopy (EDS), transmission electron microscopy (TEM) and an X-ray diffraction (XRD). With a HITACHI-S4800 field-emission SEM with 10–15 kV accelerating voltage and 8 mm working distance, the spherical-aberration corrected field emission transmission electron microscope (HRTEM) image for ZnP_2 nanowires was recorded. For the TEM images, the samples were prepared by dropping ZnP_2 nanowires in ethanol onto 200 mesh lacey carbon-coated copper grids. Furthermore, EDS was used to confirm the elements of the nanowire. Moreover, XRD samples were prepared by drying the ZnP_2 nanowire solutions on Si substrates, and the pattern was obtained with the Shimadzu XRD-6000 diffractometer equipped with Cu Kα radiation.

Conclusions

In summary, for the first time, binary lithium-reactive zinc di-phosphide (ZnP_2) nanowires were successfully synthesized *via* Bi-seeded nanowire growth *via* a solvothermal route. This synthetic method not only lowers the reaction temperature, but also enables the ZnP_2 nanowires to react with lithium and exhibit a distinguished capacity of 1415 mA h g^{-1} for the first cycle and a high Coulombic efficiency up to 89%. The stability performance was excellent because the capacity still had 1066 mA h g^{-1} after 500 cycles. Furthermore, even at high rates (4C), the capacity could still have 309 mA h g^{-1} in the performance. The great performance of lithium batteries has shown ZnP_2 nanowires as appealing nanomaterials for technological improvements in energy storage due to their nanostructure and phosphorous-rich composition. Since phosphorus has the highest theoretical capacity in sodium ion batteries among all elements, the performance of ZnP_2 in the sodium batteries can be expected.[66–68]

Acknowledgements

H.-Y. T acknowledges the financial support by the Ministry of Science and Technology through the grants NSC 102-2221-E-007-023-MY3, MOST 103-2221-E-007-089-MY3, MOST 103-2622-E-007-025, and MOST 102-2633-M-007-002.

Notes and references

1 L. Li, Z. Wu, S. Yuan and X. B. Zhang, *Energy Environ. Sci.*, 2014, **7**, 2101–2122.
2 J. Liu, D. B. Buchholz, R. P. H. Chang, A. Facchetti and T. J. Marks, *Adv. Mater.*, 2010, **22**, 2333–2337.
3 I. Shakir, M. Shahid, U. A. Rana, I. M. Al Nashef and R. Hussain, *Electrochim. Acta*, 2014, **129**, 28–32.
4 S. Siddiqui, D. I. Kim, L. T. Duy, M. T. Nguyen, S. Muhammad, W. S. Yoon and N. E. Lee, *Nano Energy*, 2015, **15**, 177–185.
5 S. A. H. Ali, A. Hussin and A. K. Arof, *J. Power Sources*, 2002, **112**, 435–442.
6 M. Majima, S. Ujiie, E. Yagasaki, K. Koyama and S. Inazawa, *J. Power Sources*, 2001, **101**, 53–59.
7 P. Schoderbock and H. P. Boehm, *Synth. Met.*, 1991, **44**, 239–246.
8 X. L. Ji, K. T. Lee and L. F. Nazar, *Nat. Mater.*, 2009, **8**, 500–506.
9 J. S. Lee, C. Lee, J. Jun, D. H. Shin and J. Jang, *J. Mater. Chem. A*, 2014, **2**, 11922–11929.
10 D. Oh, J. F. Qi, B. H. Han, G. R. Zhang, T. J. Carney, J. Ohmura, Y. Zhang, Y. Shao-Horn and A. M. Belcher, *Nano Lett.*, 2014, **14**, 4837–4845.
11 H. B. Wu, J. S. Chen, H. H. Hng and X. W. Lou, *Nanoscale*, 2012, **4**, 2526–2542.
12 H. Xia, Z. T. Luo and J. P. Xie, *Nanotechnol. Rev.*, 2014, **3**, 161–175.
13 Y. M. Chun and H. C. Shin, *Electrochim. Acta*, 2016, **209**, 369–378.

14 Y. U. Kim, C. K. Lee, H. J. Sohn and T. Kang, *J. Electrochem. Soc.*, 2004, **151**, A933–A937.
15 Z. Q. Liang, R. J. Huo, S. H. Yin, F. Z. Zhang and S. L. Xu, *J. Mater. Chem. A*, 2014, **2**, 921–925.
16 G. A. Nazri, R. A. Conell and C. Julien, *Solid State Ionics*, 1996, **86–88**, 99–105.
17 H. Pfeiffer, F. Tancret and T. Brousse, *Electrochim. Acta*, 2005, **50**, 4763–4770.
18 J. S. Tang, C. Y. Wang, L. T. Chang, Y. B. Fan, T. X. Nie, M. Chan, W. J. Jiang, Y. T. Chen, H. J. Yang, H. Y. Tuan, L. J. Chen and K. L. Wang, *Nano Lett.*, 2013, **13**, 4036–4043.
19 J. S. Tang, C. Y. Wang, M. H. Hung, X. W. Jiang, L. T. Chang, L. He, P. H. Liu, H. J. Yang, H. Y. Tuan, L. J. Chen and K. L. Wang, *ACS Nano*, 2012, **6**, 5710–5717.
20 J. S. Tang, C. Y. Wang, F. X. Xiu, A. J. Hong, S. Y. Chen, M. S. Wang, C. F. Zeng, H. J. Yang, H. Y. Tuan, C. J. Tsai, L. J. Chen and K. L. Wang, *Nanotechnology*, 2010, **21**, 505704.
21 F. W. Yuan, H. J. Yang and H. Y. Tuan, *ACS Nano*, 2012, **6**, 9932–9942.
22 J. Hwang, C. Jo, M. G. Kim, J. Chun, E. Lim, S. Kim, S. Jeong, Y. Kim and J. Lee, *ACS Nano*, 2015, **9**, 5299–5309.
23 F.-W. Yuan and H.-Y. Tuan, *Chem. Mater.*, 2014, **26**, 2172–2179.
24 F.-W. Yuan, H.-J. Yang and H.-Y. Tuan, *ACS Nano*, 2012, **6**, 9932–9942.
25 T. Kennedy, M. Bezuidenhout, K. Palaniappan, K. Stokes, M. Brandon and K. M. Ryan, *ACS Nano*, 2015, **9**, 7456–7465.
26 X. J. Feng, J. Yang, Y. T. Bie, J. L. Wang, Y. N. Nuli and W. Lu, *Nanoscale*, 2014, **6**, 12532–12539.
27 R. X. Lin, S. C. Zhang, G. R. Liu, Z. J. Du and L. B. Kang, *Int. J. Electrochem. Sci.*, 2013, **8**, 8019–8029.
28 H. J. Tian, X. J. Tan, F. X. Xin, C. S. Wang and W. Q. Han, *Nano Energy*, 2015, **11**, 490–499.
29 J. Wang, M. J. Zhou, G. Q. Tan, S. Chen, F. Wu, J. Lu and K. Amine, *Nanoscale*, 2015, **7**, 8023–8034.
30 A. M. Chockla, J. T. Harris, V. A. Akhavan, T. D. Bogart, V. C. Holmberg, C. Steinhagen, C. B. Mullins, K. J. Stevenson and B. A. Korgel, *J. Am. Chem. Soc.*, 2011, **133**, 20914–20921.
31 J. Collier, S. Wu and D. Apur, *Energy*, 2014, **74**, 314–321.
32 S. Hasenohrl, P. Elias, J. Soltys, R. Stoklas, A. Dujavova-Laurencikova and J. Novak, *Appl. Surf. Sci.*, 2013, **269**, 72–76.
33 K. Ikejiri, Y. Kitauchi, K. Tomioka, J. Motohisa and T. Fukui, *Nano Lett.*, 2011, **11**, 4314–4318.
34 M. V. V. M. S. Kishore and U. V. Varadaraju, *J. Power Sources*, 2006, **156**, 594–597.
35 E. J. Luber, M. H. Mobarok and J. M. Buriak, *ACS Nano*, 2013, **7**, 8136–8146.
36 M. Sharma, M. Mushrush, R. J. Wright, N. Shinkel, S. Sprague, S. Rozeveld, M. Woodward, K. Kearns, P. Small and C. Todd, *Thin Solid Films*, 2015, **591**, 32–38.
37 G. W. Witmer, J. D. Eisemann, T. M. Primus, J. R. O'Hare, K. R. Perry, R. M. Elsey and P. L. Trosclair, *Bull. Environ. Contam. Toxicol.*, 2010, **84**, 698–702.
38 F. Zan and J. C. Ren, *J. Mater. Chem.*, 2012, **22**, 1794–1799.
39 S. Carenco, M. Demange, J. Shi, C. Boissiere, C. Sanchez, P. Le Floch and N. Mezailles, *Chem. Commun.*, 2010, **46**, 5578–5580.
40 S. D. Miao, T. Yang, S. G. Hickey, V. Lesnyak, B. Rellinghaus, J. Z. Xu and A. Eychmuller, *Small*, 2013, **9**, 3415–3422.
41 M. H. Mobarok and J. M. Buriak, *Chem. Mater.*, 2014, **26**, 4653–4661.
42 M. H. Mobarok, E. J. Luber, G. M. Bernard, L. Peng, R. E. Wasylishen and J. M. Buriak, *Chem. Mater.*, 2014, **26**, 1925–1935.
43 H. Hwang, M. G. Kim, Y. Kim, S. W. Martin and J. Cho, *J. Mater. Chem.*, 2007, **17**, 3161–3166.
44 G. Shen, Y. Bando, C. Ye, X. Yuan, T. Sekiguchi and D. Golberg, *Angew. Chem., Int. Ed.*, 2006, **45**, 7568–7572.
45 G. Shen, Y. Bando and D. Golberg, *J. Phys. Chem. C*, 2007, **111**, 5044–5049.
46 M. Bhushan and A. Catalano, *Appl. Phys. Lett.*, 1981, **38**, 39–41.
47 G. Shen, P.-C. Chen, Y. Bando, D. Golberg and C. Zhou, *J. Phys. Chem. C*, 2008, **112**, 16405–16410.
48 W. W. Li, L. Gan, K. Guo, L. B. Ke, Y. Q. Wei, H. Q. Li, G. Z. Shen and T. Y. Zhai, *Nanoscale*, 2016, **8**, 8666–8672.
49 C.-M. Park and H.-J. Sohn, *Chem. Mater.*, 2008, **20**, 6319–6324.
50 E. Fahrenkrug, J. Biehl and S. Maldonado, *Chem. Mater.*, 2015, **27**, 3389–3396.
51 A. T. Heitsch, D. D. Fanfair, H. Y. Tuan and B. A. Korgel, *J. Am. Chem. Soc.*, 2008, **130**(16), 5436–5437.
52 K. W. Kolasinski, *Curr. Opin. Solid State Mater. Sci.*, 2006, **10**, 182–191.
53 Y. M. Sung, W. C. Kwak and T. G. Kim, *CrystEngComm*, 2012, **14**, 389–392.
54 F. D. Wang, A. G. Dong, J. W. Sun, R. Tang, H. Yu and W. E. Buhro, *Inorg. Chem.*, 2006, **45**, 7511–7521.
55 H. Yu and W. E. Buhro, *Adv. Mater.*, 2003, **15**, 416–419.
56 X. Lu, D. D. Fanfair, K. P. Johnston and B. A. Korgel, *J. Am. Chem. Soc.*, 2005, **127**, 15718–15719.
57 H. Geaney, E. Mullane and K. M. Ryan, *J. Mater. Chem. C*, 2013, **1**, 4996–5007.
58 V. A. Rubtsov, E. M. Smoljarenko, V. M. Trukhan, V. N. Yakimovich and L. K. Orlik, *Cryst. Res. Technol.*, 1989, **24**, 55–58.
59 D. R. Rao and A. Nayak, *J. Mater. Sci.*, 1992, **27**, 4389–4392.
60 F.-W. Yuan and H.-Y. Tuan, *Cryst. Growth Des.*, 2010, **10**, 4741–4745.
61 H. Lee, S. Choi, S. Choi, H.-J. Kim, Y. Choi, S. Yoon and J.-J. Cho, *Electrochem. Commun.*, 2007, **9**, 801–806.
62 K. Kang, Y. S. Meng, J. Bréger, C. P. Grey and G. Ceder, *Science*, 2006, **311**, 977–980.
63 A. Jossen, *J. Power Sources*, 2006, **154**, 530–538.
64 Y. M. Sun, X. L. Hu, W. Luo, F. F. Xia and Y. H. Huang, *Adv. Funct. Mater.*, 2013, **23**, 2436–2444.
65 A. Ueda, M. Nagao, A. Inoue, A. Hayashi, Y. Seino, T. Ota and M. Tatsumisago, *J. Power Sources*, 2013, **244**, 597–600.
66 W. Li, S.-L. Chou, J.-Z. Wang, J. H. Kim, H.-K. Liu and S.-X. Dou, *Adv. Mater.*, 2014, **26**, 4037–4042.
67 W.-J. Li, S.-L. Chou, J.-Z. Wang, H.-K. Liu and S.-X. Dou, *Nano Lett.*, 2013, **13**, 5480–5484.
68 W.-J. Li, Q.-R. Yang, S.-L. Chou, J.-Z. Wang and H.-K. Liu, *J. Power Sources*, 2015, **294**, 627–632.